engineering proceedings

MDPI

Proceeding Paper

Assessment of Lunar User PVT Performances Tightly Coupling Moonlight Signal with IMU Measurements †

Yoann Audet [1,*,‡], Michele Ceresoli [2,‡], Floor T. Melman [1], Dimitrios V. Psychas [1], Richard D. Swinden [1,*], Cosimo Stallo [3], Monica Gotta [3] and Javier Ventura-Traveset [4]

[1] European Space Research and Technology Centre (ESTEC), European Space Agency, Keplerlaan 1, 2201AZ Noordwijk, The Netherlands; floorthomas.melman@esa.int (F.T.M.); dimitrios.psychas@esa.int (D.V.P.)
[2] Department of Aerospace Science and Technology, Politecnico di Milano, Via La Masa 34, 20156 Milan, Italy; michele.ceresoli@polimi.it
[3] European Centre for Space Applications and Telecommunications, Fermi Ave, Harwell, Didcot OX11 0FD, UK; cosimo.stallo@esa.int (C.S.); monica.gotta@esa.int (M.G.)
[4] ESA Toulouse, Centre Spatial de Toulouse, European Space Agency, 18 Avenue Edouard Belin, 31401 Toulouse, France; javier.ventura-traveset@esa.int
* Correspondence: yoann.audet@ext.esa.int (Y.A.); richard.swinden@esa.int (R.D.S.)
† Presented at the European Navigation Conference 2025 (ENC 2025), Wrocław, Poland, 21–23 May 2025.
‡ These authors contributed equally to this work.

Abstract

With the renewed interest in lunar exploration, evidenced by the increasing number of planned missions over the past decade, space agencies are investing in dedicated lunar communication and navigation systems, such as the European Space Agency's (ESA) Moonlight Lunar Communication and Navigation System (LCNS), to support various types of missions. Other space agencies, such as NASA and JAXA, are also foreseeing to deploy similar infrastructure, which will all be interoperable according to the LunaNet Specification. One of the critical phases in both human and robotic lunar exploration is the landing of spacecrafts on the Moon's surface. This operation is complex and challenging, as demonstrated by recent crashes like the Luna25 lander from the Russian Space Agency or the Intuitive Machine private lander. Reliable positioning capabilities during descent are among the various services offered by dedicated lunar navigation systems and shall enable safe and reliable landing to a 90 metres 3-sigma landing accuracy from a target point, as defined by the Global Exploration Roadmap Critical Technology Needs. Faulty landings can be due to several causes. This paper examines the achievable positioning accuracy for a lander targeting the Moon's South Pole using satellite-based navigation services like Moonlight and how the impact of faulty sensors (such as a faulty IMU) can be mitigated using Moonlight LCNS.

Keywords: lander; Moonlight; lunar-PNT; IMU

Check for updates

Academic Editor: Tomasz Hadaś

Published: 3 March 2026

Copyright: © 2026 by the authors. Licensee MDPI, Basel, Switzerland. This article is an open access article distributed under the terms and conditions of the Creative Commons Attribution (CC BY) license.

1. Introduction

In recent years, there has been a significant resurgence of interest in lunar exploration, driven by an increasing number of planned missions and ambitious initiatives aimed at returning to the Moon. This renewed focus on lunar exploration has prompted space agencies worldwide to develop robust communication and navigation systems specifically tailored for both human and robotic missions on the lunar surface. Among these initiatives, the Moonlight program [1], developed by the European Space Agency (ESA), is one example

of such infrastructure which should be available towards the end of the decade. As part of the LunaNet framework [2], an effort for interoperability between systems from different providers, NASA, JAXA, which are both developing similar systems, and ESA are collaborating to provide interoperable communication and navigation services from the different constellations to future lunar explorers.

A critical aspect of lunar exploration is the intricate process of landing spacecraft on the Moon's surface. Although this achievement was first accomplished decades ago, recent incidents, such as the crash of the Luna25 lander by the Russian Space Agency [3], or the more recent fail of the Intuitive Machine lander [4], have highlighted the complexities and challenges involved in this endeavor. Successfully navigating a spacecraft through the lunar environment requires exceptional precision and accuracy, particularly during the crucial final descent phase. In response to these challenges, there is a growing recognition of the need for reliable methods to guide and position landers during their final approach and touchdown.

To address this imperative, the International Space Exploration Coordination Group (ISECG) has identified key technological requirements in its Global Exploration Roadmap [5] which would allow secure landing and development of lunar economic activities. Among these critical needs is the achievement of a landing accuracy of 90 m with a 3-sigma level of confidence from the designated nominal target point. Attaining such precision is considered essential for ensuring the reliability and success of lunar landing operations, thereby underscoring the importance of advancements in navigation technologies designed for lunar missions.

This paper aims to investigate proposed lunar navigation systems and evaluate the achievable positioning accuracy for landers targeting the Moon's South Pole. Specifically, the study examines the effectiveness of utilizing dedicated satellite-based navigation services, such as the Moonlight LCNS constellation, and IMU (Inertial Measurement Unit), in a tightly coupled manner, to enhance the precision of lunar landings. Additionally, for the last phase of the EDL, an altimeter is assumed. The focus is also made on how the navigation information from the LCNS constellation can mitigate faulty IMU which has caused failure of several space missions over the decades.

2. Simulation Framework

2.1. Moonlight Lunar Communication and Navigation System (LCNS)

2.1.1. Moonlight/LCNS Constellation

In line with previous work [6,7], the considered LCNS constellation is designed assuming four satellites are available on ELFOs (Elliptical lunar frozen orbits) separated in two planes. Table 1 provides the orbital elements in the ICRF (International Celestial Reference Frame) reference frame valid for 1 January 2027.

Table 1. Keplerian elements of the LCNS ELFO orbits. RAAN stands for the right ascension of the ascending node. Please note that values here are not optimized and thus do not represent the final Moonlight constellation.

Satellite Id	**1**	**2**	**3**	**4**
Semi-Major Axis (km)	9750.73	9750.73	9750.73	9750.73
Eccentricity	0.6383	0.6383	0.6383	0.6383
Inclination (°)	54.33	54.33	61.96	61.96
Argument of pericenter (°)	55.18	55.18	121.7	121.7
RAAN (°)	277.53	277.53	59.27	59.27
True Anomaly (°)	123.42	0	180	0

https://doi.org/10.3390/engproc2026126033

The constellation parameters in this publication are derived by ESA based on internal studies, and they are not considered fully optimized. Therefore, better performances in terms of geometry and availability are expected as part of the Moonlight program. The timing of the landing trajectory is optimized to ensure visibility of the four satellites during the landing.

2.1.2. LCNS Navigation Payload

Similar to the Earth-GNSS concept, the user positioning in the service volume is based on TDOA (time difference of arrival) and FDOA (frequency difference of arrival) between the satellite broadcasting the navigation signal and the user receiver. The selected on-board clock for the LCNS navigation payload is the MiniRAFS [8].

The Signal-in-Space Error (SISE), which is the system contribution to the User Equivalent Ranging Error (UERE), is modeled using a realistic Orbit Determination and Time Synchronization (ODTS) simulator, providing the time series. The simulator also offers the Signal-in-Space Accuracy (SISA) time series, which is the SISE time series prediction provided by the system. This process involves two distinct steps. First, a simulation step is performed to propagate the satellite's orbit using a precise dynamical model and an observation model for measurement generation. The second step involves estimating, via generated measurements, each satellite's position, velocity, and clock through a batch (4 days) least-squares estimator. Further information on the ODTS simulation is presented in previous work [6,7,9].

2.2. Lander Scenario

2.2.1. Landing Trajectory

The considered mission scenario consists in the spacecraft descent from the apocenter of an elliptical Low Lunar Orbit (LLO) (100 × 30 km altitude) down to 3 m above the targeted landing site close to the Lunar South Pole. The trajectory reproduces the common scheme of lunar landings, with the initial coasting phase ending at the periselene of the LLO, where the Main Breaking Burn (MBB) is initiated at full thrust to reduce the orbital velocity. This maneuver lasts until the lander reaches the Pitch-Up Gate (PGA), at an altitude of about 1 km, where thrust is re-oriented towards the vertical direction and the Hazard Detection and Avoidance (HDA) sensors and routines are activated. A final powered descent is foreseen for the last few hundreds of meters and ends before the final vertical descent at the Vertical Gate (VGA), 3 m above the surface and with null horizontal velocity.

The trajectory was generated following the expected profile of the Argonaut mission [10], using an indirect optimization technique for the main braking phase, and a semi-analytical guidance for the final approach [11]. Once an initial guess is available, the final approach trajectory is recomputed using a direct optimization strategy ensuring continuity with the previous phase. The lander is assumed to have an initial mass of 7000 kg, a maximum thrust of 18,000 N, an a specific impulse of 330 s. After the MBB phase, the thrust is assumed to be throttable between 5000 N and 12,000 N, with a maximum throttle rate of 400 N/s. The duration of the coasting arc is of 3431 s, whereas the entire thrusting arc lasts 584 s. The generated trajectory is available in Figure 1.

https://doi.org/10.3390/engproc2026126033

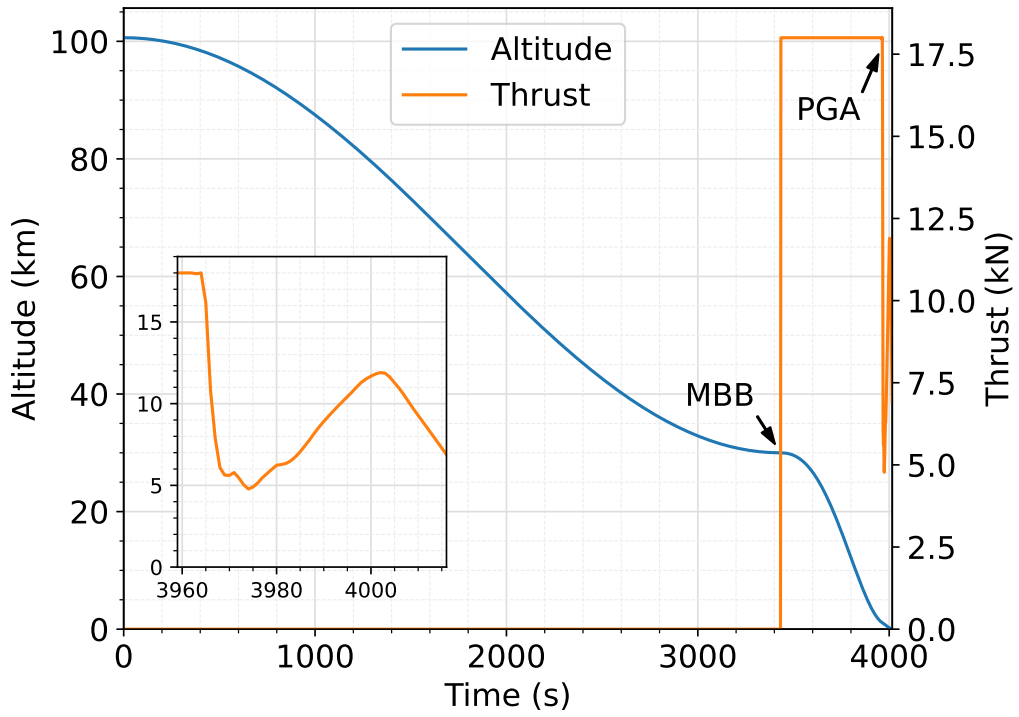


Figure 1. Landing altitude and thrust profiles.

2.2.2. Lander Payload

The lander is equipped with two antennas on either side, inclined at 45 degrees relative to the zenithal direction, to maximize the visibility of the Moonlight constellation signals as described in Section 2.1.2. These antennas are connected to a Moon GNSS receiver, which is based on the model of a space-borne receiver, adapted to receive S-band signals, and designed to acquire and track the LunaNet AFS broadcasted by Moonlight LCNS. Concerning the clock, we assume the receiver embarks a space qualified OCXO (Oven Controlled Chrystal Oscillator) for timing purposes [12].

Concerning the IMU, the choice was made to reproduce, with high fidelity, the MS-IMU3025 from MEMSENSE [13] as it was designed for space applications. Table 2 presents the characteristics of the IMU. This type of IMU is not representative of the best high-grade IMU that most landers are equipped with. However, our goal is to demonstrate that even without being in the best conditions, having an IMU helps the achievable positioning accuracy of the lander during the EDL (Entry, Descent and Landing) phase in nominal conditions. For the sake of completeness, a second high-grade IMU is also studied to check the performance improvement. The parameters of this IMU are also presented in Table 2. This IMU is based on the LN-200HPS model from Northrop Grumman [14]. This IMU was used in several deep space and rover missions (Mars Rovers such as Spirit or Hayabusa 2 probe) and is designed for high performance in a space related context. Unfortunately, due to the high commercial sensitivity and dual use nature of this sensor, not all the information for the model is available in the public datasheet. Unavailable parameters are thus downscaled from the MS-IMU3025 model by a factor of 10 (this was arbitrary assumed).

Table 2. Simulated IMU parameters.

Parameter		MS-IMU3025			LN-200HPS
Range (g)		5			40
Resolution (g)		2.3283×10^{-10}			N/A
Bandwidth (Hz)		50			N/A
Non-orthogonalities (°)	Cross-axis	0.006			0.005
	Misalignement	0.006			0.005
axis		x	y	z	all-axis
Bias repeatability (g)	mean	395.0×10^{-6}	395.0×10^{-6}	446.0×10^{-6}	300
	std	225.0×10^{-6}	225.0×10^{-6}	303.0×10^{-6}	N/A
	max	2.0×10^{-3}	2.0×10^{-3}	3.0×10^{-3}	N/A
Bias instability (g)	mean	2.6×10^{-6}	2.6×10^{-6}	1.1×10^{-6}	N/A
	std	0.7×10^{-6}	0.7×10^{-6}	1.1×10^{-6}	N/A
Bias random walk (g)	mean	0.0	0.0	0.0	N/A
	std	3.0×10^{-6}	3.0×10^{-6}	3.0×10^{-6}	N/A
Velocity random walk (g)	mean	17.3×10^{-6}	17.0×10^{-6}	23.7×10^{-6}	3.5×10^{-6}
	std	0.9×10^{-6}	0.7×10^{-6}	1.3×10^{-6}	N/A
Scale factors (ppm)	mean	133.0	140.0	391.0	100
	std	24.0	27.0	304.0	N/A
	max	190.0	215.0	1270.0	N/A
Scale factor non-linear (ppm)	mean	2609.0	2609.0	2609.0	N/A
	std	66.0	66.0	66.0	N/A

3. Positioning Model

This analysis is based on an absolute positioning model making use of LCNS and IMU measurements. Since the LCNS component has been discussed in our previous works [6], we focus here on the IMU component and the tight-coupling approach. This section focuses on the IMU simulation framework and the tight coupling approach.

3.1. IMU Framework

Figure 2 represents the architecture used to simulate the IMU measurement generation. From the Lander trajectory simulation, presented in Section 2.2.1, two types of acceleration are extracted:

1. Non-gravitational accelerations: these accelerations are the one that can be measured by the IMU.
2. Gravitational accelerations: these accelerations cannot be measured by the IMU. However, they can be obtained at filter level using a gravitational model. In the filter, they are obtained from a reduced gravitational model of the Moon approximating the Moon gravity model up to degree and order 40.

Figure 3 presents the general framework to simulate the accelerometer from an IMU. The simulation platform developed to generate measurements for the selected IMU is based on this general framework. However, some terms were neglected due to the difficulty to model accurately the behavior of the sensors in real condition. The two neglected parameters are the vibration and temperature noises. Those terms are in a simulation difficult to model accurately and are not the dominant factor of the IMU error budget. The simulator is taking as input the non-gravitational accelerations and simulates the IMU reading by simulating the biases, noises, and quantization affecting the IMU measurements.

Table 3 reports the value used for each model. The noises and biases are thus initialized in a random way based on the mean and std value. All those errors are initialized as white noise. However, based on the integrators in Figure 3, the final noise contribution on the IMU measurement is from a different color (i.e., integrating a white noise produces brown noise). Angular-rate measurements from the IMU are not considered in this analysis.

Table 3. Three-dimensional Position error for INS-LCNS and altimeter positioning (considering convergence period).

3D Position Errror	Mean Error	95th Perc.
	No IMU	
before altimeter activation	34.82 m	35.34 m
after altimeter activation	11.86 m	13.21 m
	MS-IMU3025	
before altimeter activation	28.31 m	32.62 m
after altimeter activation	10.19 m	13.28 m
	LN-200HPS	
before altimeter activation	28.27 m	32.37 m
after altimeter activation	10.21 m	13.11 m

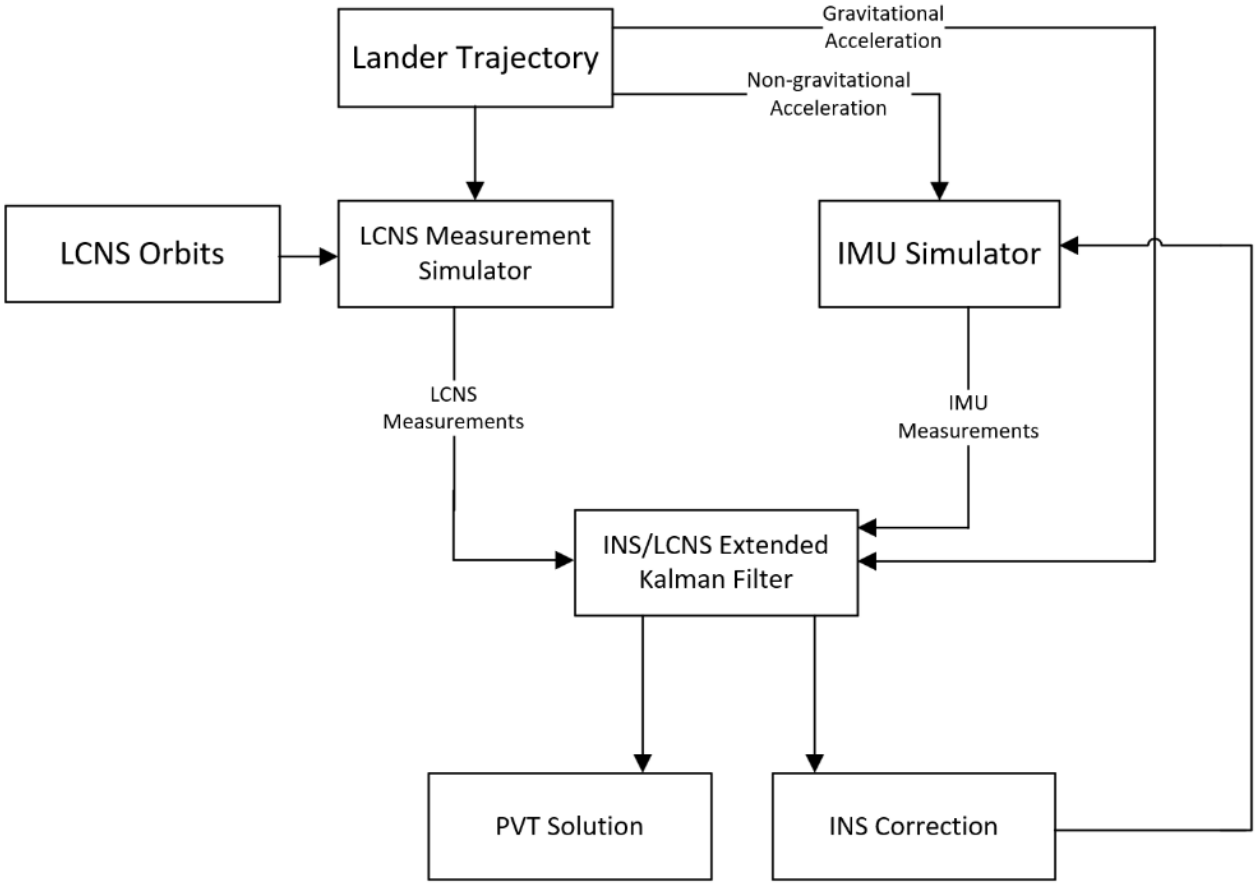


Figure 2. Simulation framework for the IMU/LCNS tight integration.

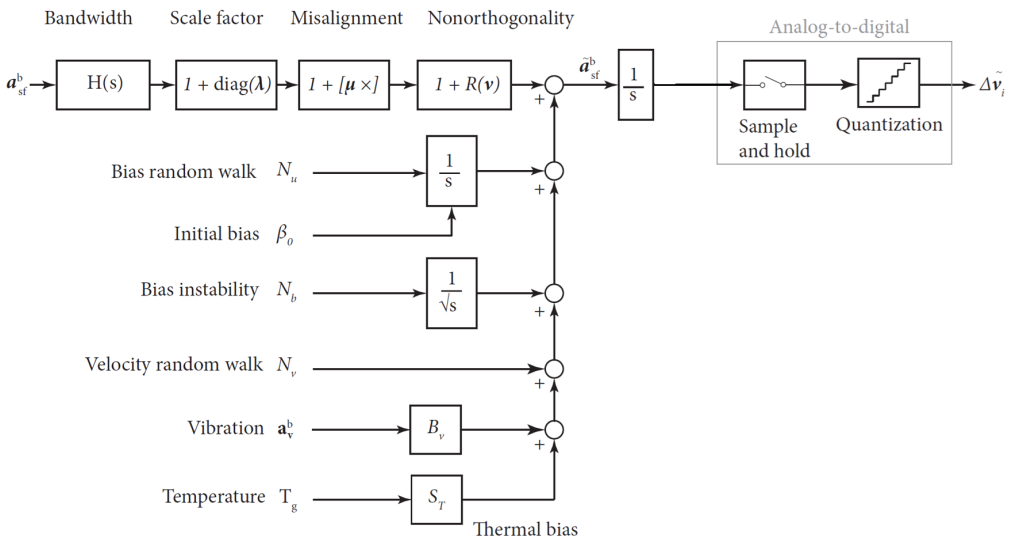


Figure 3. IMU's accelerator modeling.

3.2. Faulty IMU Scenarios

In this section, we present the two faulty scenarios that could occur during a lander's EDL. In real-world applications, a sensor can fail in multiple ways; it is thus difficult to have an exhaustive analysis of each fault mode of the sensor. In this contribution, the analysis is limited to two different scenarios that occured in previous missions.

3.2.1. Faulty Scenario 1: Faulty IMU Mounting

The first scenario investigated in the current contribution is one replicating the crash of the PROTON-M rocket at Baikonour cosmodrome in Kazaksthan [15]. The fault was most likely caused by the angular velocity sensors installed upside-down when integrated in the rocket. This led to the crash of the rocket moments after the launch.

In our simulation frame, this fault is quite simple to implement by increasing the value of the mounting error term. In this casel, we set the value to 180 degrees, meaning the IMU is installed upside-down in the lander.

3.2.2. Faulty Scenario 2: Schiaparelli Representative Case

The second scenario is caused on a replicate of the Schiaparelli case which crashed on Mars in 2016 [16]. The crash was caused by a saturation of the gyroscope after the parachute deployment leading to a saturation of the accelerometer and a wrong integration of the lander trajectory. In the nominal case, the lander should have fired its retrorockets from 10 m above the ground to 3 m and then fall on the surface. Due to the false integration, the boosters were fired 3 km above the surface for a few meters. The lander then fell from 3 km altitude onto the surface, leading to the total loss of the mission.

Based on this study case, even though a moon lander is not equipped with parachutes, the second faulty scenario represents a case where the IMU is assumed to be saturated by the thrust of the lander during the descent.

3.3. Navigation Filter Tight Coupling

The navigation performance is assessed using an Error-State Extended Kalman Filter (EKF) leveraging a tight-coupling approach between the LCNS radio-navigation measurements, the onboard altimeter and the IMU. The measurement model and coupling approach using the altimeter (similar approach as in [6]) and the LCNS measurements are presented in previous work [6]. The tight IMU integration algorithms are presented in Figure 2. Concerning the different frame for the IMU and the platform, as well as the lever-arm, they

are assumed to be calibrated and are thus neglected in this analysis. Both antenna and IMU centers are thus considered collocated. The state-vector of the designed EKF is (as described in [17]):

$$\boldsymbol{x} = \begin{bmatrix} \boldsymbol{r} \\ \boldsymbol{v} \\ \boldsymbol{b_a} \\ \boldsymbol{c} \end{bmatrix} \tag{1}$$

with $\boldsymbol{r}$ being the 3×1 position vector of the lander, $\boldsymbol{v}$ being the 3×1 velocity vector of the lander, $\boldsymbol{b_a}$ being the 3×1 acceleration bias in the IMU measurements, and $\boldsymbol{c}$ being the two states clock representation of the lander clock bias and drift.

Regarding the evolution of the accelerometer bias, the bias is modeled by a first-order Gauss Markov process (independent on the 3 axes), which reads as (for the 1D case):

$$b_a(t_n) = e^{-\beta \Delta t} b_a(t_{n-1}) + \eta(t_n) \tag{2}$$

Concerning the position and velocity, the propagation is based on a two-body model. The clock dynamic model is a two-state model based on clock bias and drift.

Finally, the propagation model reads as:

$$\boldsymbol{x}(t_n) = F\boldsymbol{x}(t_{n-1}) = \begin{pmatrix} I_{3x3} & I_{3x3}\Delta t & 0 & 0 & 0 \\ 0 & I_{3x3} & 0 & 0 & 0 \\ 0 & 0 & e^{-\beta \Delta t} I_{3x3} & 0 & 0 \\ 0 & 0 & 0 & 1 & \Delta t \\ 0 & 0 & 0 & 0 & 1 \end{pmatrix} \boldsymbol{x}(t_{n-1}) \tag{3}$$

with Δt as the sampling interval, $I_{n \times n}$ as the identity matrix of size n, β as the first-order Gauss Markov process parameter ($1/\beta$ is the time constant), and F as the propagation model. The value of β changes based on the IMU type. The value is set to 1 Hz for the MS-IMU3025 and 0.5 Hz for the LN-200HPS.

The formulated measurement and stochastic models read as:

$$E(\rho) = H\boldsymbol{x}, \quad D(\rho) = R \tag{4}$$

with ρ being the measurement vector composed of pseudorange and doppler measurements, H the geometry matrix, and R the variance matrix of the measurement errors. The definition of H and R is given in [6]. $E(\cdot)$ and $D(\cdot)$, respectively, denote the expectation and dispersion operators. The Extended Kalman Filter equations used for are presented in [7]. The altimeter integration in the filter is presented in [6].

4. Results and Discussion

4.1. Precision Landing with LCNS and IMU

First, Table 3 presents the positioning performance for a landing scenario without using an IMU on the investigated scenario. Using the IMU, results are presented in Figure 4 and Table 3. We can observe the main driver in that simulation is the inclusion of the altimeter when the estimated altitude reaches 2 km. The grade of the IMU does not seem to significantly improve the performances in this case. This might be due to several factors and the fact that there is always four satellites in view during the studied landing trajectory.

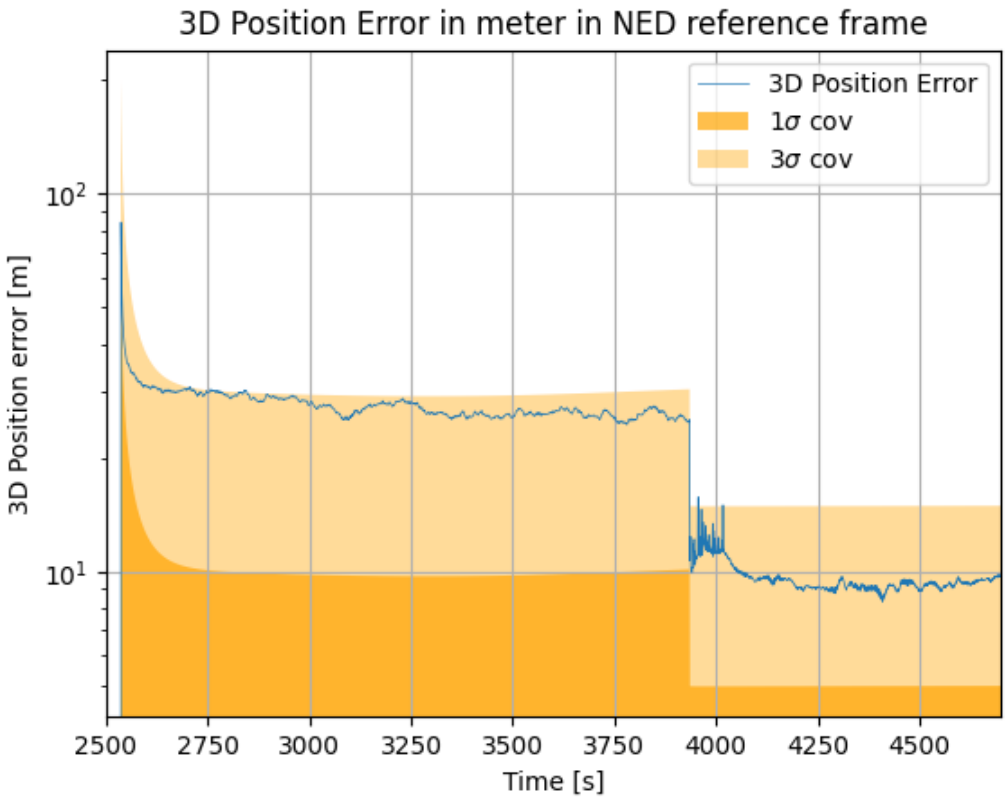


Figure 4. Three-dimensional positioning accuracy (shown in blue color) of the lander over time making use of the MS-IMU3025 IMU. The confidence intervals are shown with light and dark orange colors.

4.2. Precision Landing with LCNS Under Faulty IMU Assumption

The fault is introduced here at 3433 s into the landing on the (Micro-Electro-Mechanical System) IMU model.

In both cases, Figures 5 and 6, the IMU fault has an impact of the achievable positioning accuracy. However, the landing accuracy is here limited to 100 m accuracy during this phase. According to the Schiaparelli fault report [16], in real-worl conditions, a similar failure lead to several kilometers errors. Moreover, some simulation have been performed on this scenario using the presented simulation architecture and relying only on the IMU. The final landing error ranges between 8 km (for an ideal IMU) up to 100 km for the MEMS IMU. This shows the benefit of LCNS when it comes to reliability of the overall landing system. Additionally, we can see that when the altimeter is activated, the navigation filter can recover the right solution after some convergence time.

From an integrity point of view, when the IMU is faulty, the performance degradation is such that the final positioning accuracy outputted by the filter is worse than the LCNS alone solution in Table 3. In the tight coupling integration scheme, both solutions, using the IMU measurements and without including them, can be computed in parallel with a very minimal additional computational cost. If two solutions are maintained in parallel, they can be compared at any instant during the landing trajectory to detect faults of any of the systems. This can be part of a higher-level integrity concept to ensure safer landing operations in the future. Additionally, comparing the two solutions can help detect any mismodelling in the measurement and/or dynamic models.

https://doi.org/10.3390/engproc2026126033

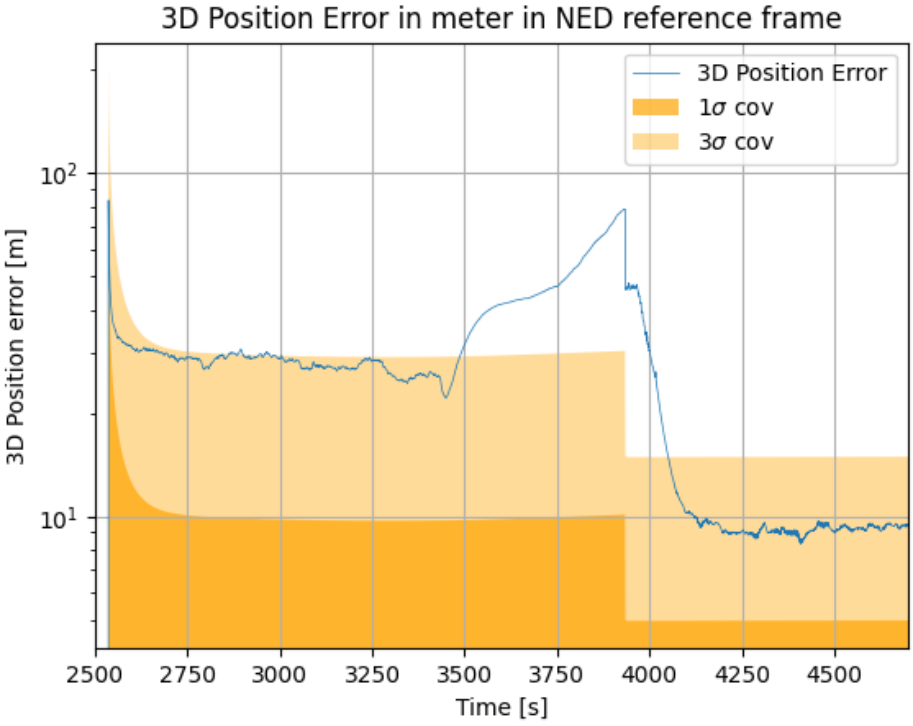


Figure 5. Three-dimensional position error for Fault 1 (for the legend, refer to Figure 4 caption).

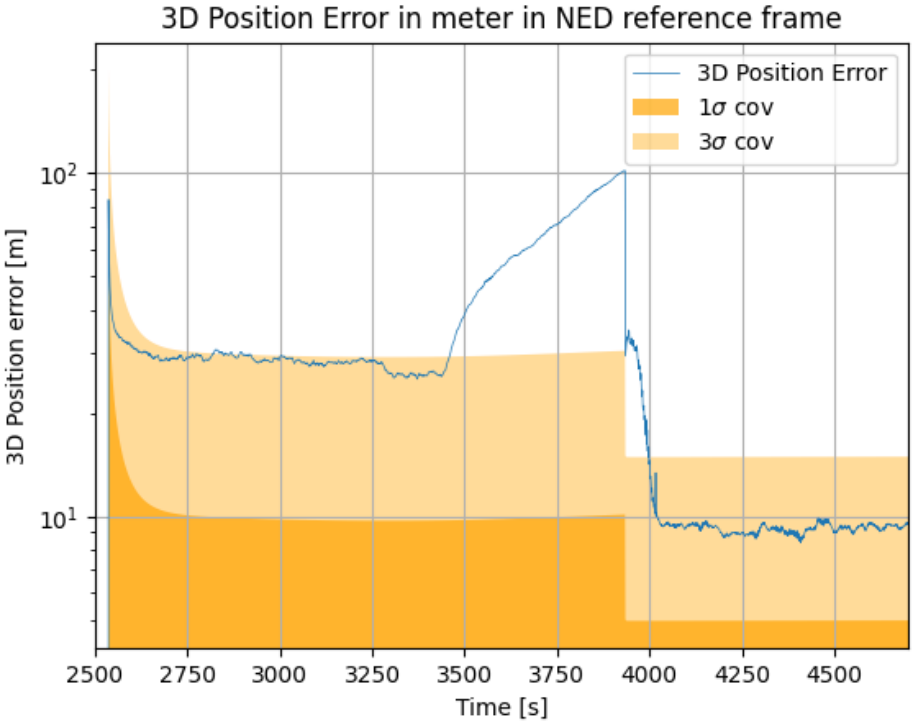


Figure 6. Three-dimensional position error for Fault 2 (for the legend, refer to Figure 4 caption).

5. Conclusions

According to the assessment conducted by the ISECG and detailed in the Global Space Exploration Roadmap [5], one of the primary challenges identified for future lunar exploration is ensuring accurate navigation for landers. Although Earth-GNSS can be utilized above Medium Earth Orbit (MEO) [1], during Earth to Moon transfer orbits, and in lunar orbits, it does not offer sufficient coverage (the signal reception is limited to the

near side) and the antenna accommodation and pointing of the lander is more complicated. The proposed Lunar Communication and Navigation System (LCNS) constellation aims to address this issue by providing navigation capabilities in lunar orbit, enabling real-time positioning, velocity, and timing (PVT) for various orbital, landing, and surface users.

This contribution aims at gaining insight on the achievable performances for a lander assuming it is equipped with an IMU and able to receive the AFS signal coming from the Moonlight LCNS constellation. The combination of using LCNS and an IMU will slightly improve the achievable positioning accuracy of the lander compared to using just LCNS.

The second purpose of the current contribution was to check, in case of a failure of the IMU sensor, whether the presence of the LCNS measurements could counter-balance this fault and still preserve the lander from total loss. Two different cases were studied for this purpose based on realistic failures modes that have occurred in the past. In both cases, the performances of the navigation are greatly degraded. However, the presence of LCNS measurements can still mitigate a part of this error and reduce the chances of complete loss of the mission.

As a next step, this analysis can be developed including measurements coming from a visual navigation (absolute or relative) payload which is expected to further enhance the positioning performance of the lander. Additionally, as briefly aforementioned, the integrity concept of a landing operation is a key factor. A further natural step would be to investigate what would be the performances assuming a failure of the LCNS constellation and whether other sensors (IMU, Visual-based navigation, etc.) can counter-balance this effect to ensure safe operations. Finally, the current analysis is only presenting two fault cases. In future work, a complete fault tree analysis should be performed to address all cases.

Author Contributions: Conceptualization, Y.A., M.C., D.V.P., F.T.M. and R.D.S.; methodology, Y.A. and M.C.; software, Y.A. and M.C.; validation, Y.A., M.C., D.V.P. and F.T.M.; writing—original draft preparation, Y.A. and M.C.; writing—review and editing, Y.A.; project administration, C.S., M.G., R.D.S. and J.V.-T. All authors have read and agreed to the published version of the manuscript.

Funding: This research received no external funding.

Institutional Review Board Statement: Not applicable.

Informed Consent Statement: Not applicable.

Data Availability Statement: The data presented in this study are available upon request from the corresponding author.

Conflicts of Interest: The authors declare no conflicts of interest.

Abbreviations

The following abbreviations are used in this manuscript:

AFS	Augmented Forward Signal
BPSK	Binary Phase Shift Key
EDL	Entry, Descent and Landing
EKF	Extended Kalman Filter
ELFO	Elliptical Lunar Frozen Orbit
ESA	European Space Agency
FDOA	frequency Difference Of Arrival
HDA	Hazard Detection and Avoidance
ICRF	International Celestial Reference Frame
IMU	Inertial Measurement Unit

ISECG	International Space Exploration Coordination Group
LCNS	Lunar Communication and Navigation System
LLO	Low Lunar Orbit
MBB	Main Breaking Burn
MEMS	Micro-Electro-Mechanical System
OCXO	Oven Controlled Chrystal Oscillator
ODTS	Orbit Determination and Time Synchronization
PGA	Pitch-Up Gate
PNT	Positioning, navigation and timing
RAAN	Right Ascension of Ascending Node
SISA	Signal-In-Space Accuracy
SISE	Signal-In-Space Error
TDOA	Time Difference Of Arrival
UERE	User Equivalent Ranging Error
VGA	Vertical Gate

References

1. Giordano, P.; Malman, F.; Swinden, R.; Zoccarato, P.; Ventura-Traveset, J. The Lunar Pathfinder PNT Experiment and Moonlight Navigation service The Future of Lunar Position, Navigation and Timing. In Proceedings of the 2022 International Technical Meeting of The Institute of Navigation, Long Beach, CA, USA, 25–27 January 2022; Volume 2022, pp. 632–642. [CrossRef]
2. *Draft LunaNet Interoperability Specifications*; Technical Report; NASA: Washington, DC, USA, 2022. Available online: https://ntrs.nasa.gov/citations/20220004317 (accessed on 21 June 2022).
3. Walsh, A. Russia's Luna-25 Spacecraft Crashes into Moon. *BBC*, 20 August 2023. Available online: https://www.bbc.com/news/world-europe-66562629 (accessed on 2 March 2026).
4. Foust, J. Altimeter Problems, Lighting Challenges Caused IM-2 Lunar Lander to Fall on Its Side. *SpaceNews*, 13 May 2025. Available online: https://spacenews.com/altimeter-problems-lighting-challenges-caused-im-2-lunar-lander-to-fall-on-its-side/ (accessed on 2 March 2026).
5. ISECG. The Global Exploration Roadmap. International Space Exploration Coordination Group. 2019. Available online: https://www.globalspaceexploration.org/wp-content/uploads/2019/12/2019_GER_Technologies_Portfolio_ver.IR-2019.12.13.pdf (accessed on 13 June 2023).
6. Audet, Y.; Melman, F.T.; Psychas, D.V.; Swinden, R.; Ventura-Traveset, J. Positioning of a Lunar Lander using a dedicated Lunar Communication and Navigation System assuming realistic ODTS performances. *Eng. Proc.* **2025**, *88*, 74.
7. Audet, Y.; Melman, F.; Molli, S.; Sesta, A.; Plumaris, M.; Psychas, D.; Swinden, R.; Giordano, P.; Ventura-Traveset, J. Positioning of a Lunar Surface Rover on the South Pole Using LCNS and DEMs. *Adv. Space Res.* **2024**, *74*, 2532–2550. [CrossRef]
8. SAFRAN. *MINIRAFS RB Atomic Frequency Standard*; SAFRAN Electronics and Defense: Paris, France, 2021. Available online: https://safran-navigation-timing.com/product/minirafs-rb-atomic-frequency-standard/?model_interest__c=MiniRAFS&product_interest___single_select=Atomic+Clocks+and+Oscillators (accessed on 16 May 2025).
9. Di Benedetto, M.; Boscagli, G.; De Marchi, F.; Durante, D.; Santi, F.; Sesta, A.; Plumaris, M.; Fienga, A.; Linty, N.; Sośnica, K.; et al. An architecture for a lunar navigation system: Orbit determination and time synchronization. In Proceedings of the ESA's 8th International Colloquium on Scientific and Fundamental Aspects of GNSS, Sofia, Bulgaria, 14–16 September 2022.
10. Capolupo, F.; Rinalducci, A. Descent & Landing Trajectory and Guidance Algorithms with Divert Capabilities for Moon Landing. In Proceedings of the AIAA SCITECH 2024 Forum, Orlando, FL, USA, 8–12 January 2024; p. 0086.
11. Lunghi, P.; Di Lizia, P.; Armellin, R.; Lavagna, M. Semi-analytical adaptive guidance computation for autonomous planetary landing. *Acta Astronautica* **2022**, *195*, 265–275. [CrossRef]
12. AXTAL GmbH. *AXIOM70SL: Ultra-Low Phase Noise 10 MHz OCXO with HCMOS Output for Space Application (Space COTS Version)*; AXTAL GmbH: Mosbach, Germany, 2022. Available online: https://www.axtal.com/cms/docs/doc124949.pdf (accessed on 14 June 2022).
13. Memsense. MS-IMU3025. Available online: https://memsense.com/products/ms-imu3025/ (accessed on 22 May 2025).
14. Grumman, N. LNS-200S. Available online: https://www.northropgrumman.com/what-we-do/mission-solutions/assured-navigation/ln-200s-inertial-measurement-unit (accessed on 2 March 2026).
15. Brumfiel, G. Report: Upside-Down Sensors Toppled Russian Rocket. *npr*, 10 July 2013. Available online: https://www.npr.org/sections/thetwo-way/2013/07/10/200775748/report-upside-down-sensors-toppled-russian-rocket (accessed on 2 March 2026).

16. Tolker-Nielsen, T. *EXOMARS 2016—Schiaparelli Anomaly Inquiry*; Technical Report; ESA: Paris, France, 2017.
17. Morton, Y.J.; van Diggelen, F.; Spilker, J.J., Jr.; Parkinson, B.W.; Lo, S.; Gao, G. (Eds.) *Position, Navigation, and Timing Technologies in the 21st Century: Integrated Satellite Navigation, Sensor Systems, and Civil Applications, 2 Volume Set*; Wiley-IEEE Press: Hoboken, NJ, USA, 2020.

Disclaimer/Publisher's Note: The statements, opinions and data contained in all publications are solely those of the individual author(s) and contributor(s) and not of MDPI and/or the editor(s). MDPI and/or the editor(s) disclaim responsibility for any injury to people or property resulting from any ideas, methods, instructions or products referred to in the content.